Analyst

Accepted Manuscript

Analyst

Review Article

Applications of Coherent Raman Scattering Microscopies to Clinical and Biological Studies

Iwan W. Schie[a], Christoph Krafft[a], and Jürgen Popp[a,b]

Coherent anti-Stokes Raman scattering (CARS) microscopy and stimulated Raman scattering (SRS) microscopy are two nonlinear optical imaging modalities that are at the frontier of label-free and chemical specific biological and clinical diagnostics. The applications of coherent Raman scattering (CRS) microscopies are multifold, ranging from investigation of basic aspects of cell biology to the label-free

10 detection of pathologies. This review summarizes recent progress of biological and clinical applications of CRS between 2008 and 2014, covering applications such as lipid droplet research, single cell analysis, tissue imaging and multiphoton histopathology of atherosclerosis, myelin sheaths, skin, hair, pharmaceutics, and cancer and surgical margin detection.

Introduction

15 The current review provides an update of a previous review on Raman and coherent anti-Stokes Raman scattering (CARS) microscopy of cells and tissues.[1] Due to the huge progress and the large number of papers within the past six years, spontaneous Raman and coherent Raman microscopies are described

20 separately this time. After Freudiger *et al.*[2] and Nandakumar et al.[3] independently introduced stimulated Raman scattering (SRS) microscopy to biological samples, its popularity considerably increased and relevant SRS papers are included in this review as well.

25 Recent reviews summarized the most frequent applications of CARS and SRS. CARS microscopy was introduced as a method for high-speed, non-staining biomolecular imaging[4] and compared to Fourier transform infrared (FTIR) imaging. It was concluded that coherent Raman scattering (CRS) microscopies

30 offer advantages with respect of spatial resolution and low absorption by water; in comparison to spontaneous Raman scattering, CRS offers a significant signal enhancement, natural confocality, and no signal overlap with one-photon excited fluorescence. A tutorial summarized fundamentals and biological

35 applications of CRS.[5] Advances of CARS in detection schemes, understanding of contrast mechanisms and developments of laser sources were described together with emerging applications such as metabolite and drug imaging, and tumor identification.[6] Recent advances in multiphoton imaging – the combination of CARS

40 microscopy with other nonlinear optical imaging modalities – were summarized together with technical developments and applications in life sciences.[7] Lipids are popular targets for CARS and SRS microscopy because of their large scattering cross sections and high local concentrations in cellular lipids droplets,

45 adipocytes, nervous tissues, breast tissue, fatty liver tissue, and other lipid related pathologies. Label-free imaging by CARS and SRS microscopy was reviewed for lipid functions, metabolism

and storage[8], lipids in artificial membrane model systems, living cells, tissues and even whole organisms[9], lipid dynamics in the

50 nematode *Caenorhabditis elegans* as a genetic model[10], lipid biology in cell cultures, tissue biopsies and model organisms[11], studies of lipid-droplet biology, obesity-cancer relationship, atherosclerosis and lipid-rich biological structures[12], and diagnosis of multiple sclerosis and other myelin diseases[13].

55 Quantitative analysis in CARS is not straightforward; because on the one hand, the signal intensity depends quadratic on the concentration, on the other hand the non-resonant signal causes a distortion of the spectral line-shape due to the spectral interference between the resonant and the non-resonant

60 contribution of the 3rd-order nonlinear susceptibility $\chi^{(3)}$. Various experimental and mathematical approaches have been adopted to extract quantitative information from the CARS signal.[14] Though, in SRS non-resonant background is not generated, it is not background free. Effects such as cross-phase modulations,

65 thermal lensing, and transient absorption do occur and have some degrading effects on the image contrast.[15]

The combination of high resolution CARS microscopy with multimodal imaging was applied for dynamic monitoring of cellular processes such as lipid metabolism and storage, the

70 movement of organelles, adipogenesis and host pathogen interactions and was also used to track molecules within living cells and tissues.[16] Multiphoton microscopies use ultra short (ps to fs) pulses with high pulse energies, high repetition rates of 80 MHz, and near infrared wavelengths that are considered to be

75 minimally invasive. Relevant papers in ophthalmology that included two-photon excited fluorescence (TPEF), second harmonic generation (SHG), third harmonic generation (THG), fluorescence lifetime imaging (FLIM) and CARS were summarized.[17] Multiphoton microscopic imaging offers also

80 advantages for a wide range of pharmaceutical and biopharmaceutical applications such as material and dosage form

Analyst Accepted Manuscript

characterization, dosage form digestion and drug release, and drug and nanoparticle distribution in tissues and within live cells.[18] In regenerative medicine nonlinear optical microscopy was used in the field of tissue engineering and characterization of artificial tissue.[19] Applications of nonlinear microscopy to skin biology were also reported.[20]

Table 1 indicates the total number of CARS and SRS microscopy papers published annually, starting 2008. The numbers are based on a PubMed search. Two interesting facts can be derived: first, the number of CARS papers per year is almost constant since 2009; second, the number of SRS papers has increased since 2008. It is likely that the number of CARS related papers did not change significantly, because the number of research groups has not significantly expanded. On the other hand, the number is not dropping, which indicates that the research in established applications is on-going. The number of publications for SRS microscopy has been constantly growing, and due to the advantages of SRS, it is likely to surpass CARS microscopy in the near future.

The current review presents a selection of CARS and SRS papers in lipid droplet research, single cell analysis, tissue imaging and multiphoton histopathology of atherosclerosis, myelin sheaths, skin, hair, pharmaceutics, and cancer. A detailed review on the theory and implementation of CARS and SRS microscopies, goes beyond the scope of this review, and can be found elsewhere.[3, 21]

Year	2008	2009	2010	2011	2012	2013	2014	Sum
CARS	29	46	50	54	40	41	47	307
SRS	2	2	8	13	11	19	27	82

Table 1: Total number of CARS and SRS microscopy papers published annually starting from 2008 until December 2014. Number of published papers was determined through a PubMed search in March 2015.

Lipid Droplet Research and Single Cells Analysis

In recent years, lipid droplets (LDs) have come under scrutiny as one of the main culprits for many Western-diet related diseases, such as diabetes type 2[22], obesity[23], fatty liver disease[24], atherosclerosis[25], and many others. For a long time it was thought that cellular LDs act as neutral storage vesicles for excessive esterified lipids, and have no other cellular functions.[26] Due to substantial efforts in LD research in recent years a new picture begun to emerge of a vivid and dynamic cellular organelle that is not only responsible for storage of neutral lipids, but also protects cells from lipotoxicity,[27] is a source for membrane lipid biosynthesis,[28] protein storage and metabolism,[29] can act as hatcheries for the hepatitis C virus,[30] and can even be a marker for circulating tumor cells, as has been shown by Mitra et al.,[31, 32] using CARS microscopy.

Cellular LDs are usually visualized by fluorescent labels such as Oil Red O,[33] Nile Red,[34] and very recently BODIPY dyes[35]. Fluorescent probes, however, cannot always be used with living samples, due to induced cellular toxicity. Moreover, they are not photostable, which is an important requirement when doing long-term observations and motility tracking of cellular LDs. A particularly intriguing study by Yen et al. compared the performance of Oil Red O, Nile Red, BODIPY, and Sudan Black

with CARS microscopy, analyzing lipid storage in wild-type and mutant *C. elegans* nematodes.[36] The results show that fluorescent labels produce competing results when staining cellular lipid organelles. Not only was the quantification of LDs different between individual dyes and CARS microscopy, also differences between staining of living nematodes and fixed nematodes were observed. These kinds of studies emphasize the importance of CARS microscopy in LD research.

The ability of CARS microscopy to provide chemically specific information without the need for exogenic labels is particularly intriguing for live cell work and *in vivo* applications. Zhu et al. used CARS microscopy to investigate and to quantify a dynamic triglyceride pool in enterocytes, cells of the small intestine, during a dietary fat absorption *in vivo* and *ex vivo*.[37] In two follow-up studies by the same group it was shown that the PAT proteins, TIP47 and adipophilin, play a distinctive roll in the absorption of fat in the small intestine,[38] and that the crucial intestinal fat-metabolism enzyme DGAT1, stimulates the secretion of dietary fat from enterocytes.[39] By utilizing multiplex CARS microscopy, and detecting multiple molecular vibrations at a time, Bonn et al. showed the distribution of linolenic acid and palmitic acid in individual cellular LDs in adipocytes and HeLa cells.[40] Distinct differences in LD size and LD composition were observed between the two cell types. The differentiation of mouse embryonic fibroblast cell line 3T3-L1 into adipocyte cells has also been investigated by CARS microscopy.[41] The results showed a phenotypic heterogeneity during the differentiation of these cells, which depended on the insulin-signaling cascade.

Because the conventional implementation of CARS microscopy provides information only of a single selected molecular vibration, and omits all other molecular bonds present in the sample, Slipchenko et al. combined CARS microscopy with spontaneous Raman spectroscopy, which provides chemical information about all molecular bonds in the sampling volume, on the same optical platform.[42] By incubating cells with deuterated palmitic acid the researchers were able to determine the amounts of endogenous to exogenous fatty acids present in individual cellular LDs. Using CARS microscopy they were also able to image mouse skin *in vivo* at two different depths, visualizing glands and subcutaneous adipocytes. Raman spectroscopy on the glands and the subcutaneous adipocytes showed distinct differences in the lipid profile of both fat-rich structures, the glands having a 2.1 higher amount of saturated fatty acids than subcutaneous adipocytes. In another publication from the same group Le and co-workers used the compound Raman spectroscopy and CARS microscopy approach to identify auto-fluorescent subspecies of cellular LDs that coexist with 'neutral' LDs.[43] The expression levels of auto-fluorescent to 'neutral' LD species showed a high correlation with genotype-phenotype relation of mutant *C. elegans* nematode. A combination of Raman spectroscopy and CARS microscopy was also used by Schie et al. to determine the fatty acid composition of individual cellular LDs, which originated from oleic acid mediated protection from palmitic acid induced lipotoxicity in HepG2 cells.[44] The determined fatty acid composition in individual LDs was compared with results from gas chromatography (GC) for the same fatty acid exposure conditions. The comparison between the methods proved that the

Raman based fatty acid profiling performed equally well to GC, but allowed a fatty acid profiling on a single LDs level, which is not possible by GC. Figure 1 shows some results for this study. Figure 1a is a CARS image of LDs in hepatocarcinoma cells, which were exposed to an equal concentration of oleic and palmitic acid, i.e. 250 μM each. Raman spectra were acquired from the indicated locations. The relative concentrations of the two fatty acids in the indicated LDs were calculated from the Raman spectra based on an asymmetric least squares fitting of pure components spectra to the data. The results for the individual LDs are shown below the CARS image in a pie chart and as actual values. For comparison, the relative concentration as determined by GC analysis of the fatty acid content of a few million cells is also plotted. This approach can be beneficial where lipid profiling has to be done rapidly in single cells and with minimal sample preparation. An expansion to more than two fatty acids, *i.e.*, whole fatty acid profiling *in vivo*, is feasible. Figure 1b shows an example for the combination of the CARS microscopy with TPEF microscopy from the same publication, where peroxisome and LDs were imaged simultaneously on a multiphoton microscopy setup with consecutive Raman spectroscopy of peroxisome and LDs.
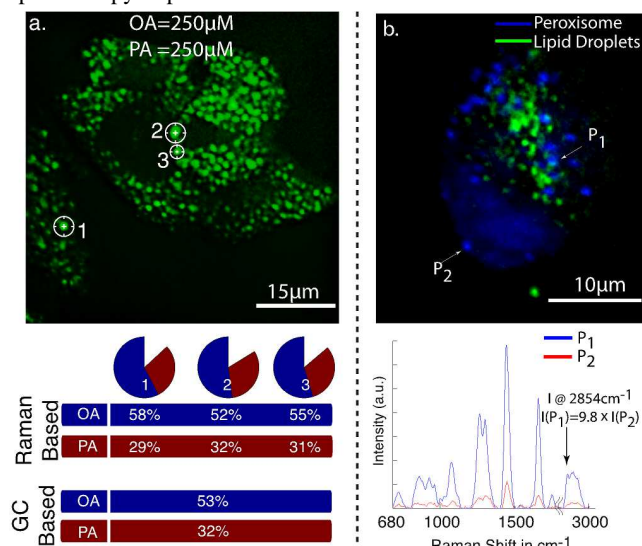

Figure 1 a. CARS image of cellular lipid droplet accumulations in HepG2 cells after the exposure to 250 μM of oleic acid (OA) and 250 μM palmitic acid (PA). Raman spectra were taken from the indicated cellular lipid droplets. The pie charts show the relative amount of oleic and palmitic acid in the individual lipid droplets determined from the Raman spectra. The percentile values are plotted below. The GC values indicate the amount for OA and PA determined from lipid droplets of millions of cells. It can be seen that the values are in good agreement. Fig. 1 b. shows a multiphoton image of HepG2 cells. The CARS signal from cellular lipid droplets is in green, and TPEF signal of green fluorescence protein expressed in peroxisome in blue. The unnormalized Raman spectra for the indicated point are shown below. The peak intensity of the CH_2 stretch vibration at 2854 cm^{-1} is 9.8 times lower from peroxisome

Lipolysis is a key process for LD and lipoprotein degradation, occurring in all eukaryotic cells. During lipolysis a triglyceride molecule is hydrolyzed into a glyceride molecule and 3 fatty acids. A visualization of this process has previously not been possible. By using multiplex CARS micro-spectroscopy, Day *et al.* imaged the digestion of glyceryl trioleate emulsion droplet by a porcine pancreatic lipase.[45] While that study was focusing on the process of triglyceride hydrolyzation, others have investigated the effects of lipolysis products of very low-density lipoprotein (VLDL) on cultured THP1-monocytes.[46] Cells exposed to VLDL lipolysis products developed cellular LDs. The degree of unsaturation inside the LDs was highly dependent on the state of the VLDL. When postprandial VLDL was used, cellular LDs contained more saturated fatty acids; when fasting VLDL was used, cellular LDs contained more unsaturated fatty acids. In a similar study Schie *et al.* investigated the effects of postprandial VLDL lipolysis products on primary hepatocytes, showing that the first cellular lipid accumulations can be observed by CARS microscopy as early as 30 min after the exposure to lipolysis products of postprandial VLDL.[47] Moreover, by using Raman spectroscopy they were able to show that the degree of fatty acid unsaturation in cellular LDs was depending on the size of the LDs. A similar effect of fatty acid unsaturation dependence on size has also been shown previously by Argov *et al.*.[48] The study of lipolysis effects is also intriguing from the point of view of lipid reducing drugs. For example, fenofibrate is a triglyceride lowering drug, which activate peroxisome proliferator-activated receptor alpha (PPARα), which in itself activates lipoprotein lipases, reduces the amounts of VLDL particle and low-density lipoprotein (LDL) particles, and increases the amounts of high-density lipoprotein (HDL) particles.[49] Using CARS microscopy Uchida *et al.* showed that the effect of fenofibrate in mice on a high-fat diet was a decrease in triglyceride supply to the small intestine, which in part was due to a decrease in dietary fatty acid absorption, and an increase in dietary fatty acid oxidation.[50] In a closely related study by the same researchers it was also shown that triglyceride storage and secretion of the small intestine is altered in obese mice.[51] Such an evaluation can also be done in an automated and quantitative way, as was shown in a study of hydrolysis in macrophages, using CARS microscopy.[52]

LD motility is an important function of the lipid organelle. There are two distinct ways of intracellular transport for LDs: active transport and passive transport.[53] Cellular transport mechanisms have been extensively studied with fluorescence microscopy, though the droplets have to be stained by an exogenic stain, potentially altering the transport mechanism; also, the dyes photobleach, allowing only a short glimpse into the motility of LDs. One of the first studies of LDs by CARS microscopy investigated the organelle motility in steroidogenic mouse adrenal cortical (Y-1) cell, observing sub-diffusional movement, and microtubule-mediated active transport.[54] More recently, Jüngst *et al.* studied the motility of LDs with CARS microscopy at video-rate speed and showed that images of LD motility can be acquired for several hours without damaging the cells.[55] As mentioned before, such long observation periods are not feasible with fluorescent-based methods because of photo bleaching. The observed average velocity for active transport in HeLa cells of more than 111 individual LDs and a total of 583 segments was 149.7 nm/s. In a follow-up study, CARS microscopy was used for a long-term label-free imaging of lipid transfer between

individual LDs.[56] The lipid-transfer directionality during LD fusion depended on the size difference between the LDs; the lipid-transfer rate, however, depended on the size difference and the diameter of the smaller LD.

The discovery that cellular LDs are involved in the production of hepatitis C virus (HCV) triggered a broad interest in LDs, also in the CARS community. Though, CARS is not able to visualize the HC virus, a combination of CARS and TPEF microscopy has been used to visualize changes in localization and phenotype of LD's and subgenomic HCV replicon RNA in living cells upon treatment with a lipid metabolism inhibitor.[57] In a follow-up publication with an addition of differential interference microscopy (DIC) to CARS microscopy, and TPEF microscopy Lyn *et al.* showed that the HCV core protein induces size increase of LDs, and also affects the directionality of microtubule-mediated LD transport in Huh7.5 cells.[58]

One of the biggest disadvantages of CARS microscopy is the presence of a non-resonant background signal that can overshadow a resonant signal from molecules present at low concentrations.[59] Though many methods were developed to overcome this problem, they have their own drawbacks and complications. SRS microscopy emerged as an alternative to CARS microscopy, because it provides the same benefits as CARS microscopy, but overcomes the typical problems of CARS. It does not have a non-resonant signal contribution, has a linear dependency on the concentration, and the generated SRS spectra are identical to spontaneous Raman spectra, which makes spectral analysis and interpretation straight forward. Although the SRS effect was observed in the early 60's,[60] and has been broadly studied and used, it gained wide popularity in biomedical research not until 2008-09.[2, 3] Applications of SRS microscopy are similar to CARS microscopy; however, it is more easily applicable to the fingerprint region, because non-resonant background contributions do not obscure the weaker Raman signals. SRS microscopy has been used to perform RNA interference screening by label-free imaging of LDs in *C. elegans* nematodes, aiding the discovery of eight new genetic regulators for fat storage.[61] Freudiger and colleagues developed a spectrally tailored-excitation SRS, which allows to distinguish between overlapping vibrational bands by spectral modulation of the multiplex excitation.[62] This approach allowed quantifying cholesterol in the presence of other lipids, and imaging of proteins, stearic acid, and oleic acid in *C. elegans*. Femtosecond-Stimulated Raman Loss microscopy was used to track LD motilities in living early drosophila embryos.[63]

A very interesting approach to study proteome synthesis was chosen by Wei *et al.*, who used a combination of SRS and deuterium labeled amino acids to detect the incorporation of amino acids into the nascent proteins of living HeLa cells, human embryonic kidney HEK293T cells, and neuron-like neuroblastoma mouse N2A cells[64]. This approach could enable a large variety of studies on protein incorporation into cells. The same group also investigated the opposite process to protein synthesis, protein degradation. In that study, instead of relying on deuterated amino acids, the researchers investigated the ratio of C^{12}-phenylalanin to C^{13}-phenylalanin isotopes to determine the incorporation of C^{13}-phenylalanin and protein turnover.[65] The protein turnover times from individual cells were comparable to published results determined by autoradiography and mass spectrometry.

Isotope labeling is not the only soft-labeling approach for Raman-based methods. Alkyne tags open up interesting alleys in CRS imaging, because those tags are small and bioorthogonal, meaning they do not interfere with cellular functions, and can label many cellular biomolecules such as nucleic acids, lipids, proteins, and glycans. Weeks et al. used alkyne-substituted oleic acid in double-resonant four-wave mixing (DR-FWM), which allows enhancing low-intensity Raman signal and reducing the non-resonant background.[66] In a follow up study, Weeks and co-workers used a combination of deuterated oleic acid and 17-octadecynoic acid with an alkyne terminal, to investigate the signal enhancement of DR-FWM in living human monocytes.[67] Alkyne tags are also very powerful in SRS because they exploit the silent region of the Raman spectrum, between 1800 and 2800 cm^{-1}, not interfering with any Raman vibration.[68] Another SRS report of this labeling approach showed that alkyne tagging allows unprecedented analytical options on individual living cells, such as *de novo* synthesis of DNA, RNA, proteins, phospholipids and esterified fatty acids.[69]

The majority of publications in CARS microscopy and the early SRS publications were primarily looking at the broad high-wavenumber region between 2800 and 3100 cm^{-1}, because on the one hand, the scattering cross-section of those vibrations is significantly higher than the cross-section of the low-wavenumber region, below 1800 cm^{-1}; on the other hand, the local concentration of CH_2 can be much higher than the concentration of other molecular bonds. From the informational point of view, the low-wavenumber region is spectroscopically more interesting, due to the presence of the majority of molecular vibrations. Zhang *et al.* showed that it is possible to investigate the low-wavenumber region with SRS microscopy, exploiting a much larger number of Raman active vibrations.[70] Single polytene chromosomes were imaged in salivary glands of drosophila melanogaster and two mammalian cells, i.e. HEK-293, a human embryonic kidney, and MCF-7 breast cancer carcinoma cell line during their cell cycles. By plotting the intensities of the 785 cm^{-1} and the 1090 cm^{-1} vibration they were able to show the distribution of polytene DNA in the nucleus, also proteins at the 1655 cm^{-1} amide I vibration, and lipids at 2845 cm^{-1} CH_2 stretch vibration. Of course, the whole vibrational region can be exploited by spontaneous Raman spectroscopy in imaging mode, e.g. point or line scanning.[44] However, the acquisition time in spontaneous Raman microscopy ranges from a few minutes to a few hours, and in the presented approach the acquisition times were between 10 and 30 s.

Tissue Imaging and Multiphoton Histopathology

CRS-based methods are uniquely qualified to acquire large, label-free images of tissue *in vivo*, *in vitro*, and from pathological tissue sections.[71-73] Besides CARS and SRS signals, tissue structure and the chemical composition of tissue give rise to other nonlinear optical phenomena. Second harmonic generation, and two-photon excitation fluorescence can readily be acquired without further modifications to a CARS setup. The SHG signal is generated in non-centrosymmetric molecular structures such as

collagen fibers or crystals deposits. TPEF, on the other hand, is generated from endogenous components of the extracellular matrix, such as elastin and pyridinic coenzymes, such as NADPH, but also intra-cellular flavin coenzymes,[74] and exogenously applied labels. Hence, it is practical to include those multiphoton microscopy modalities when studying tissue specimens. Nowadays, several multiphoton modalities are often used in one study to provide more information about the sample. THG microscopy has also been applied for tissue imaging,[75, 76] but it remains to be shown, if THG provides any additional information that is not covered by the other modalities.

The capability of label-free tissue analysis is illustrated in figure 2, where CARS and SHG microscopy were used to image porcine cartilage tissue. Chondrocyte cells, which were visualized with CARS microscopy, are shown in blue, and the collagen of the extracellular matrix, which was visualized with SHG microscopy, is shown in green. A subsequent analysis from points of interest by Raman spectroscopy indicates a distinct signature of collagen in the extracellular matrix and cellular LD accumulations in chondrocytes. This approach could have significant benefits for investigating cartilage tissue damages in patients, and for quality control in artificial tissue fabrications, because it allows visualizing the morphology of the tissue and provides full chemical information from the tissue without damaging it.

In the next paragraphs we will discuss the application of CRS microscopies and other multiphoton microscopies in disease diagnostics and label-free pathology for atherosclerosis, myelin sheaths, skin, hair, pharmaceutics, and tumor identification, and surgical margin detection.

Atherosclerosis

According to the global status report on noncommunicable diseases, released by the World Health Organization (WHO) in 2010, Cardiovascular Diseases (CVDs) are the number one causes of death world wide, accounting for a third of all deaths (17.3 million people) in 2008.[77] Atherosclerotic CVD is a special form of arteriosclerosis, and the most common CVD. It is a complex inflammatory disease of the artery wall,[78] which according to Glass and Witztum, results from interaction between modified lipoproteins, monocyte-derived macrophages, T cells, and cellular elements of the arterial wall.[79] The emerging plaque formations consist of macrophages loaded with lipids, accumulations of apoptotic cells, debris, cholesterol crystals, and is accompanied by collagen overgrowth.[80] Atherosclerotic plaques develop over a long time, and stay asymptomatic for many years. Due to their relative small size, methods such as Magnetic Resonance Imaging and Computed Tomography have difficulties to detect plaque formations, especially in the early and intermediate stages. Other methods, such as Intravascular Ultrasound and Optical Coherent Tomography do not provide any chemical specific information from the arteries, making the data evaluation cumbersome.

The detections of the early and intermediate atherosclerotic lesions can particularly benefit from the different modalities of
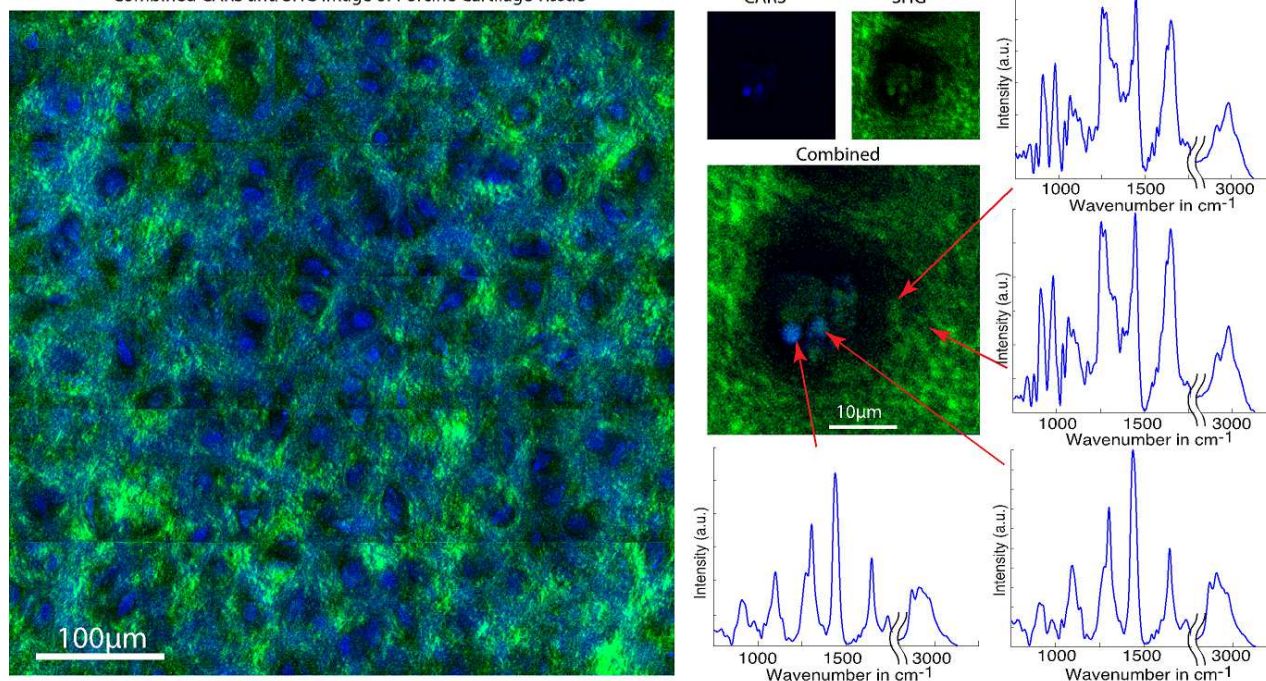

Figure 2: Multiphoton image of porcine cartilage. The CARS signal, in blue, shows the distribution of chondrocyte cells in the unstained cartilage tissue. The SHG signal, in green, shows the distribution of the extracellular matrix in the cartilage tissue. The chondrocytes are embedded in cavities of the extracellular matrix, which are called the lacuna. Raman spectra have been taken from the indicated locations of the cartilage tissue. The spectra of chondrocytes have a high resemblance with esterified lipid spectra. This can especially be seen on the presence of the triglyceride ester peak (C=O) located at 1740 cm⁻¹; it is a strong indicator for the presence of intracellular lipid droplets. The spectra of the extracellular matrix, on the other hand, are similar to spectra of collagen, especially recognizable on the presence of the two pronounced compound bands of proline and hydroxylproline, locate 857/876 cm⁻¹ and 920/240 cm⁻¹.. (Courtesy of Prof. Dr. Huser, University of Bielefeld, Germany and Dr. Schie, IPHT, Jena, Germany).

multiphoton microscopy, because multiphoton microscopy allows a label-free visualization of many hallmarks of atherosclerosis. Cells, lipid depositions, and cholesterol crystals can be detected by CARS microscopy, fibrotic formations and mineralization by SHG microscopy, and elastin, which is an integral part in scar tissue, by TPEF microscopy. There has been an extensive research effort to establish multiphoton microscopy as an emerging new technology that can provide unprecedented possibilities for the detection of atherosclerotic plaques.

The American Heart Association (AHA) released a recommendation for the pathological classification of histological atherosclerotic lesions, which correlates the appearance of the lesions to clinical imaging studies.[81] To show that multiphoton microscopy is capable to correctly identify and to correlate different stages of atherosclerotic lesions Wang *et al.* analyzed artery walls from 24 Ossabawa pigs of control animals by multiphoton microscopy, and compared it to artery walls from a metabolic syndrome group.[82] In addition, the multiphoton microscopy data was correlated to H&E staining of the same lesions. A quantitative analysis of lipid and collagen depositions in thickened intima of different lesions showed that both, lipid and collagen content increased dramatically in lesions Type IV in comparison to lesions Type I, with the ratio between lipid and collagen markers decreasing with increasing lesion type. Others have developed their own metric to analyze the atherosclerotic plaque burden on artery walls, *i.e.* based on the ratio of signal intensity for each of the modalities to their respective total image means.[83] The value is then combined to an optical index for plaque burden of that region. Based on this approach it was possible to distinguish between healthy and atherosclerotic regions in arteries of myocardial infarct susceptible Watanabe heritable hyperlipidemic (WHHLMI) rabbits of different ages. Multiplex CARS microscopy, covering the wavenumber range between 2650 cm^{-1} and 3050 cm^{-1} has been applied to identify lipids in aortic tissue of $ApoE^{-/-}$ mice.[84] Based on the spectral information it was possible to identify four distinct lipid morphologies: intra and extra cellular lipid deposits, and needle- and plat-shaped lipid crystals. It was also possible to characterize the lipid plaque profiles in $ApoE^{-/-}$ mice exposed to statins, which are cholesterol-lowering drugs. Similar needle-shaped lipid crystals in $ApoE^{-/-}$ mice have also been observed by Lim *et al.*.[85] In a subsequent study from the same group hyperspectral CARS microscopy was used to investigate atherosclerotic plaques in artery walls of ApoE deficient mice, showing that there is a twofold increase of the lipid area in the intimal-plaque region, and a fourfold decrease in the collagen distribution in mice on cholesterol-rich Western diet, in comparison to mice on a normal diet.[86] A study on stented coronary arteries under different diet and stent deployment conditions, concluded that stents have a negative influence on the collagen development in the neointima, when compared to the artery walls peripheral to the stent.[87] Moreover, it was found that drug-eluting stents have an inhibitory effect on the collagen development in arteries. Hyperspectral SRS combined with SHG has also been applied to study cholesterol crystals in artery walls, as a potential biomarker for atherosclerosis.[88] The majority of the cholesterol crystals were found to be composed of cholesterol monohydrates; needle-shaped cholesterol crystals that have also been observed in other multiphoton microscopy studies had a varying lipid composition. An important step towards *in vivo* Raman spectroscopy and CARS microscopy investigation of atherosclerotic plaques has been performed by Matthäus *et al.*, who utilized a Raman fiber-probe to acquire Raman spectra from various positions within the artery walls in a living rabbit, and correlated the chemical information to CARS images from the same regions in the rabbit.[89]

Myelin Sheaths

Myelin sheaths are a dielectric material surrounding the axons of nerve cells, and enabling faster signal conduction. The dry mass of myelin sheaths mainly consist of 70 % to 85 % of lipids, and the rest of proteins,[90] and it is this high lipid content in the myelin sheaths that gives the white appearance to the white matter of the brain. Demyelination of the sheaths is a hallmark for many neurodegenerative diseases such as multiple sclerosis, leukodystrophie, Guillain–Barré syndrome, and others. Myelin sheaths can also be affected by traumatic damage, which can destroy or impede the proper function of signal conduction. The *in vivo* investigation of myelin sheaths, however, has been quite challenging, due to lack of appropriate dyes for *in vivo* studies. Label-free methods, such as CARS microscopy, could have a substantial impact on the understanding of basic myelin sheaths properties and de- and remyelination processes.

In a pilot study, CARS microscopy was used to investigate a demyelinating crush injury of the sciatic nerves in living Sprague-Dawley rats at different time points post injury.[91] Immediately following the injury animals had a significantly decreased sciatic functional index, which is the indicator for the function of the sciatic nerve. Moreover, the CARS signal from the myelin filaments that was present prior to the induced trauma disappeared following the injury. Two weeks after injury, CARS signal of myelin sheaths recovered, with an increase in the myelin sheaths thickness and the total thickness of the fiber. These observations underline the unique abilities of CARS microscopy to follow label-free the remyelination of nerve fibers after injuries, and opens up a broad alley to study post injury recovery of the myelin sheaths.

The CARS signal depends on the orientation between the molecular bonds of interest and the polarization of the excitation beams. If the polarizations of the excitation beams are oriented along the CH_2 group symmetry axis, which is perpendicular to the hydrocarbon chain, the signal is maximized.[92] This effect is also observed in myelin sheaths, where the generated CARS signal intensity depends on the orientation of myelin sheaths and the excitations polarization, resulting in increased complexity for morphological analysis. Bélanger *et al.* addressed this problem by utilizing circularly polarized excitation, reducing the polarization effect to a minimum.[93] An investigation of acrolein-mediated myelin damage showed that the effect of acrolein was observed in the paranodal region in a calcium dependent and calcium independent case.[94] Here, CARS microscopy was combined with immunofluorescence imaging to show that the ratio between the axon diameter and the length of the node of Ranvier is increasing with increasing acrolein exposure time and acrolein concentration. Paranodal splitting was also observed and quantified by CARS microscopy in that same study. The

researchers concluded that acrolein has a high damaging potential on the myelin sheaths and could be an important factor in multiple sclerosis pathogenesis. Imitola *et al.* applied a combined approach of video-rate reflectance and confocal fluorescence microscopy with CARS microscopy to investigate demyelination and neurodegeneration in brain slice of animals with experimental autoimmune encephalomyelitis (EAE).[95] The EAE animals showed a very low CARS signal intensity even in myelinated regions, indicating demyelination in these mice. The analysis of knock-in mice with GFP expression in microglia revealed that microglia colocalize with areas that show increased demyelination, supporting the notion that microglia play a pivotal role in neurodegeneration.

The key parameter that describes the myelination and demyelination state is the g-ratio, which is the ratio of the axon diameter to fiber diameter, assessing the thickness of the myelin sheath. It is straightforward to determine this value in a histopathological sample using CARS microscopy. However, the assessment in a living animal is not that straight forward, due to significant moving and breathing artifacts, even with video-rate imaging. It is, therefore, highly desirable to be able to determine the g-ratio based on a single coronal image slide. Bèlange *et al.* proposed a solution to this problem by showing that if one plots the g-ratio distribution from a coronal section, the g-ratio is skewed. This, however, is not the case for g-ratio values above the median that give a good indication of the real g-ratio.[96] The research concluded that the g-ratio is not always adequate to describe the axon morphology, especially when the induced damage in the axons is too large.

Fu *et al.* used CARS, TPEF microscopy, and confocal Raman spectroscopy to investigate the initiation of demyelination in EAE induced animals at different stages: onset, peak acute, and remission.[97] The initiation of demyelination and the retraction of paranodal myelin have been observed at the onset and at the border of acute demyelination. Immunofluorescence labeling indicated that during the onset of EAE T-cells and macrophages begin to infiltrate the spinal cord tissue. The analysis with Raman spectroscopy of the myelin sheaths showed a degradation of the myelin lipids and an increase in the intermolecular chain disorder. Others have proposed an approach for longitudinal multiphoton microcopy imaging of de- and remyelination,[98] and an automated approach to investigate the local organization of myelinated axons by 2D Fourier transform analysis of the CARS imaging data.[99]

Skin, Hair, and Pharmaceutics

Due to their easy access skin and hair are the ideal samples for CRS microscopies and other multiphoton microscopies, opening new ways to investigate different properties of creams, shampoos, and other cosmetic products. Cosmetic companies are interested to understand and to characterize different properties of their products. Due to the small size of the molecules of interest, fluorescent probes are not an option to investigate a variety of properties, such as transport and absorption in skin or hair. The penetration depth, the chemical stability, and the interaction with different biological layers of skin and hair are some of the key aspects cosmetic and pharmaceutical companies are interested in. Up until now, such information was not easily available. CRS can

truly revolutionize the way to investigate a variety of properties of cosmetic and pharmaceutical formulations in living organisms or tissue models alike.

The effects of optical clearing agents such as glycerol or dimethyl sulfoxide (DMSO) are not very well understood. Especially the alternating effect of optical clearance agents on the collagen matrix is of interest to insure that no tissue-damage occurs. Zimmerley *et al.* have quantitatively investigated DMSO clearing dynamics in skin, using CARS and SHG microscopy.[100] The study suggests that DMSO affects the ordered collagen structure by changing the interspace distance of the fibrils on a submicron scale, reducing the SHG signal intensity. In a similar study, the same researchers investigated the distribution and the concentration of water and d-glycine in the cortex region of human hair fibers,[101] showing that water accounts for ~34 % content by volume, and that externally applied d-glycine is homogeneously distributed throughout the hair. This study emphasizes that CARS microscopy has the unique ability to investigate the absorption, transport, and interaction of small molecules in hair; information that previously was not attainable.

According to Saar et al.,[102] SRS microscopy application to skin imaging in living specimen was restricted for two reasons: first, slow lock-in amplifiers, which were previously used; second, low collection efficiency of objective lenses, which was due to high scattering inside the tissue and the loss of signal photons. To overcome these shortcomings, Saar and co-workers developed a fast lock-in amplifier, and a modified collection scheme. It was determined that the backscattering of photons in tissue occurs over an area with a diameter of 5 mm, whereas the aperture of a typical objective is only 1-2 mm.[102] This discrepancy reduces the signal collection by more than 90 %. To overcome this problem a photodetector was installed directly at the front aperture of the objective lens, which resulted in a collection efficiency of more than 28 % of total number of photons used to illuminate mouse skin. This modification together with a faster lock-in amplifier allowed following the penetration of the drug trans-retinol and of DMSO in a living mouse and human skin, respectively. A study investigating the skin-penetration properties of ibuprofen and ketoprofen in a propylene glycol solution showed different penetration pathways with distinct transport rates for both molecules.[103] Moreover, a formation of drug crystals at the tissue surface during the initial stages of the process was observed. Such a crystal formation has also been seen by others, who also examined the absorption properties of micro/nanoparticles in skin by a combination of SRS microscopy and fluorescence imaging.[104] Heuke and co-workers used multiphoton microscopy to comprehensively characterized human skin sections of 32 individuals, laying a solid foundation for future identification of pathology related changes in skin in clinical applications.[105]

A very interesting approach to overcome non-resonant background contributions in CARS microscopy was developed by Chowdary *et al.*, and termed Nonlinear Vibrational Interference Imaging (NIVI).[106] With this approach Benalcazar and Boppart investigated skin and were able to distinguish between stratum corneum, epidermis, dermis and hair follicle, based on the spectral difference in the 2800 to 3000 cm^{-1} region in porcine skin.[107] A combination of CARS, SHG, and TPEF has been used to image human skin.[108, 109] Mittal *et al.* have shown

that SRS microscopy can identify squamous cell carcinoma, and is sensitive to nuclear atypical cells and cell keratinization, providing superior information in comparison to reflectance confocal microscopy.[110]

Not only is the information about the properties of creams important to pharmaceutical companies, but also mechanisms of new drug-delivery pathways, and a precise understanding of the distribution of active ingredients and excipients in tablets and pills. CARS microscopy has been used to visualize and follow the dissolution of tripalmitin-based solid oral dosage forms, containing the drug theophylline anhydrate, in real time.[111] For the first time, it was possible to observe that the solid lipid extrusion prevented the formation of theophylline hydrate. Slipchenko and co-workers used SRS-, CARS-, and Raman microscopy to investigate the distribution of the pharmaceutically active compound amlodipine besylate, which is a blood pressure lowering drug, and excipients in tablets of six different manufacturers.[112] Based on the image analysis it was possible to show that the distribution of the drugs does not vary between the manufacturers, however, the distribution and the amounts of excipients do vary significantly, see Figure 3. Active pharmaceutical ingredients in tablets have also been studied by broadband CARS microscopy.[113] A combination of CARS microscopy and Raman spectroscopy was also used to investigate deuterated drugs, which exhibit bands in the Raman-silent region, and do not overlap with biological spectra.[114] Raman spectra and single band CARS intensities of different drug concentrations were measured in a two-way micro-fluidic channel and showed a linear correlation to the drug concentration. Raman spectroscopy was able to detect drug concentrations down to 50 mM; CARS was able to detect DMSO-dissolved C-deuterated naphthyl-isoquinoline down to concentrations between 50 and 100 mM.
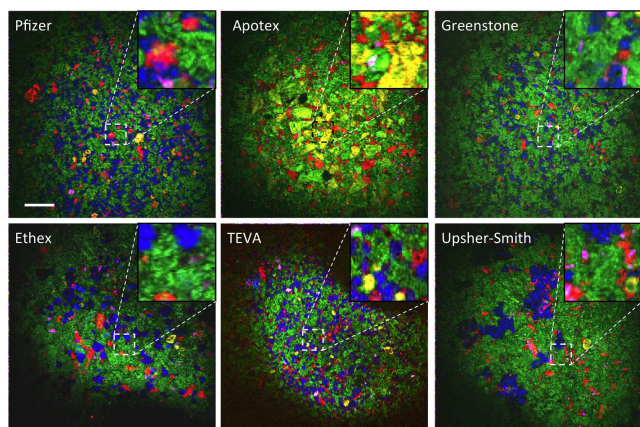

Figure 3 Large-area images acquired with SRS microscopy of amlodipine besylate containing tablets from different pharmaceutical companies. The drug and excipients present in the tablet can be identified by their respective colors, *i.e.* microcrystalline cellulose (green), dibasic calcium phosphate anhydrous (blue), amlodipine besylate (red), sodium starch glycolate (yellow), and magnesium stearate (magenta); the Apotex tablets also contained microcrystalline cellulose and lactose. Scale bar is 200 μm. (Image is courtesy of Prof. Dr. Cheng and Dr. Slipchenko, Purdue University, USA, Adopted from Slipchenko *et al. Analyst*, 2010, **135**, 2613-2619

Tumor Identification and Surgical Margins

Surgical margins, also known as normal tissue margins and tumor-free margins, are boundaries between normal and malignant tissue that can be visually determined by the surgeon, or are established through histopathology. The positive surgical margin indicates that there is still malignant tissue present and is frequently associated with a reduced disease-free survival.[115] The size of the margins is highly controversial, and also depends on the location in the body.[116, 117] The detection of those boundaries is the key aspect in surgical oncology and is directly correlated to the recurrence of a tumor. Despite this importance, the technological approach to detect these margins has not seen much change for many decades. If a surgeon does not establish margins directly, a histopathological analysis on a biopsy sample from the region of interests is performed. For histopathological analysis a stain is applied, to enhance contrast between components, e.g. cell nuclei, cytoplasm, and connective tissue. Based on the morphology a pathologist can derive information about tumor margins. It would be more favorable to apply such a stain directly during the surgery, but due to toxicity of the stains that is not easily possible.

CRS in combination with other multiphoton microscopies could have a significant impact in this area, because they are capable to distinguish between normal and malignant tissue label-free at diffraction-limited resolution, and have the capability to be a reliable guide for surgical margins during a surgery. It is not an overstatement to say that in the coming decades we will see some profound changes in the way surgeons and pathologists will identify surgical tumor margins. Figure 4 shows a compound multiphoton image of pathological brain tissue, and a comparison to H&E staining. The resemblance between the two images is remarkable.
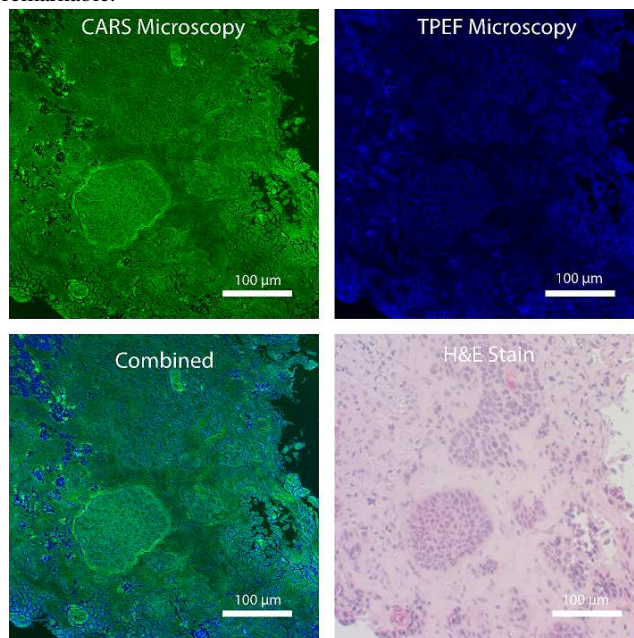

Figure 4 shows an image of porcine brain tissues, using CARS microscopy and TPEF microscopy. The combined images show comparable results to H&E staining of the same tissue. (Image is courtesy of Dr. Meyer, IPHT-Jena, Germany.)

It has been frequently shown that multiphoton microscopy has unique capabilities to identify and characterize differences in the histopathology of various diseases. For example, *ex vivo* tissue sections of basal cell carcinoma were investigated with multiphoton microscopy and spontaneous Raman spectroscopy by Vogler *et al.*.[118] The research suggests that the presence of lipid accumulations could have beneficial effects on the growth of the basal carcinoma. In a follow-up study, large basal cell carcinoma sections of size up-to (0.9 x 7.5) mm were acquired, allowing for a potential correlation to optical coherent tomography and other imaging modalities.[119] Yang *et al.* developed a visual pattern recognition approach for CARS microscopy to distinguish between breast cancer lesions and normal lesions based on the presence of fatty and fibrous structures.[120] Moreover, the researcher established an automated machine learning based approach to differentiate between different breast cancer subtypes, where morphological features such as the distribution of cell nuclei were used for the discrimination. A combination of multiphoton microscopy with Raman- and FTIR-imaging spectroscopy was used to image neurohistological pig brain slides.[121] The comparison between the label-free methods and histopathological H&E staining of the same slides showed strong morphological agreement.

Meyer and co-workers have shown how powerful the combination of the different multiphoton modalities can be in identifying advanced carcinoma of the hypopharynx, larynx, and the left tonsil in a clinical case study with three patients.[122] The researchers concluded that the information from the multiphoton microscopy surpasses that of conventional H&E staining. The analysis of multiphoton images revealed an increase in NADH/NADPH in the dysplastic epithelium in comparison to normal tissue, which is an indicator for upregulated cell activity; information that cannot easily be determined with conventional histopathology. Moreover, not only an increase in lipid content was observed in the dysplastic epithelium, but also a decrease in SHG signal intensity, which was correlated to a decrease in collagen content and to a reduced ordering in the collagen structure. Similar promising results have been shown by others, who investigated lung carcinoma lesions with multiphoton microscopy, and separated between normal, desmoplastic, and tumor tissue based on multiphoton microscopy.[123] Renal tumors have also been investigated by a combination of CARS, TFEF and SHG.[124] The multimodal images gave detailed insight in cancer morphology and composition, enabling to discern between normal kidney tissue, tumor, and necrosis. In a preliminary study CRS was used to investigate the histopathology of brain, liver, lung, ovary, spleen tissue, skin with stratum corneum, and stratum basale.[125] Similarly to Meyer *et al.*[121], they also compared different brain regions to H&E stains, showing identical information of CRS imaging and H&E. In a ground-breaking follow-up study, Ji and colleagues used SRS microscopy to delineate between normal and cancerous brain tissue of mice ex vivo on pathological slides and *in vivo*.[126] In this publication the researchers made a giant leap towards clinical application of SRS microscopy, by showing how well SRS microscopy can differentiate between cancerous and normal brain tissue in living animals. The tumor border and the infiltration of individual cells into normal tissue was precisely visualized; the bright field image of the same region shows no contrast at all. This study demonstrates the importance and the possibilities of label-free chemical microscopy for clinical applications, as a guide in surgical procedures.

Multiplex CARS microscopy has also been used for brain tissue imaging.[127] Camp Jr. *et al.* developed a modified broadband CARS (BCARS) approach, which is based on a heterodyne amplification using the non-resonant signal and a signal transformation based on the time-domain Kramers-Kronig transform. This approach not only enhances the signal, but also allows reconstructing BCARS spectra that are identical to spontaneous Raman spectra.[128] The covered spectral region in these experiments was between 500 and 3500 cm^{-1}, with a resolution of less than 10 cm^{-1}. This approach greatly enhanced the BCARS spectra and enabled an acquisition speed of a few seconds for 300×300 pixels size images, being superior to spontaneous Raman spectroscopy by at least 2 orders of magnitude. The researchers used this approach to image healthy murine liver and pancreatic tissue, and compared xenograft brain tumors with normal brain tissue, producing stunning label-free images of nucleic acid, proteins, and lipid distributions.

Conclusions

Clinical translation of CRS microscopies has enormous benefits for the medical community and early in vivo disease diagnostics, because it provides non-invasively label-free information about the molecular content of a sample at diffraction-limited resolution with high chemical sensitivity and specificity. The technical barriers that must be overcome for a clinical translation were reviewed and strategically outlined by Tu *et al.*.[129] The operation of an envisioned system should incorporate coherent Raman micro-spectroscopy for identifying vibrational biomolecular markers of a disease and single frequency (or hyperspectral) Raman imaging of these specific biomarkers for real time *in vivo* diagnostics and monitoring. However, the clinical applications of coherent Raman microscopy are partially delayed due to the lack of dedicated and easy-to-use instruments, fiber optic probes for coupling with endoscopes, and automatic algorithms for data processing and evaluation.

The majority of CARS and SRS microscopes are in-house built setups that require well-trained personnel for operation. Recently, Olympus (USA) and Leica Microsystems (Germany) introduced the first commercially available CARS microscopes in 2009 and in 2010, respectively. JenLab (Germany) introduced a scanner with TPEF and SHG, integrated into a moveable arm for the investigation of skin. An upgrade for CARS is also offered. Thorlabs (USA) provides a multiphoton microscope, which includes an option for CARS microscopy. Key elements are laser systems that generate spatially and temporally synchronized, high intensity picosecond laser pulses that can be coupled to laser-scanning microscopes. Innovative laser concepts for CRS were developed based on all-fiber laser systems that are compact, inexpensive, and enable turn-key operation.[130] These are ideal light sources for broader dissemination of the technique such as implementation into a clinical environment. Such a fiber laser was coupled to a laser-scanning microscope that was optimized for simultaneous multimodal nonlinear imaging (TPEF, SHG and

CARS), and optical throughput of near infrared light.[131] Affordable, robust and easy-to-use instruments for CRS microscopies are crucial to move the methods from the physics lab to users in medicine, biology, and chemistry.

The challenge for CARS fiber-probes are to conserve the spatial and temporal overlap of the pump and the Stokes pulse during propagation through fiber, to scan the pulses rapidly over the region of interest, to efficiently collect the backward scattered signal, and to match its size for insertion into the working channel of endoscopes. An important design consideration is the suppression of optical nonlinearities in the delivery fiber. A miniaturized CARS microscope was developed for imaging of spinal chords in living animal.[132] Another CARS probe for tissues used a scanning mirror for imaging.[133] A coherent Raman endoscope that provides SRS images at seven frames per second has also been described.[134]

Images obtained by CRS microscopies provide morphological information of cell and tissue architecture based on chemical contrast of molecular vibrations. This information can be utilized for cell and tissue identification and disease recognition. Algorithms for data processing need to be developed for objective and automated classification to complement histopathologic diagnoses. Further progress in these fields will contribute to increasing number of clinical and biological applications of coherent Raman microscopies in the near future.

Acknowledgements

Notes and references

a Leibniz-Institute of Photonic Technology, Albert-Einstein-Straße 9, 07745 Jena, Germany. Fax: +49 3641 206399; Tel: +49 3641 206306; E-mail: christoph.krafft@ipht-jena.de
b Institute of Physical Chemistry and Abbe Center of Photonics, University Jena, Helmholtzweg 4, 07743 Jena, Germany

1. C. Krafft, B. Dietzek and J. Popp, *Analyst*, 2009, 134, 1046-1057.
2. C. W. Freudiger, W. Min, B. G. Saar, S. Lu, G. R. Holtom, C. He, J. C. Tsai, J. X. Kang and X. S. Xie, *Science*, 2008, 322, 1857-1861.
3. P. Nandakumar, A. Kovalev and A. Volkmer, *New Journal of Physics*, 2009, 11, 033026.
4. M. Hashimoto, T. Minamikawa and T. Araki, *Curr. Pharm. Biotechnol.*, 2013, 14, 150-158.
5. C. Krafft, B. Dietzek, M. Schmitt and J. Popp, *J Biomed Opt*, 2012, 17, 040801.
6. C. L. Evans and X. S. Xie, in *Annual Review of Analytical Chemistry*, 2008, vol. 1, pp. 883-909.
7. T. Meyer, M. Schmitt, B. Dietzek and J. Popp, *Journal of Biophotonics*, 2013, 6, 887-904.
8. Y. Yu, P. V. Ramachandran and M. C. Wang, *Biochim. Biophys. Acta Mol. Cell Biol. Lipids*, 2014, 1841, 1120-1129.
9. A. Zumbusch, W. Langbein and P. Borri, *Prog. Lipid Res.*, 2013, 52, 615-632.
10. A. Folick, W. Min and M. C. Wang, *Curr. Opin. Genet. Dev.*, 2011, 21, 585-590.
11. T. T. Le, S. H. Yue and J. X. Cheng, *J. Lipid Res.*, 2010, 51, 3091-3102.
12. T. T. Le and J. X. Cheng, *J. Innov. Opt. Health Sci.*, 2009, 2, 9-25.
13. Y. Fu, T. M. Talavage and J.-X. Cheng, *Expert opinion on medical diagnostics*, 2008, 2, 1055-1065.
14. J. P. R. Day, K. F. Domke, G. Rago, H. Kano, H. O. Hamaguchi, E. M. Vartiainen and M. Bonn, *J. Phys. Chem. B*, 2011, 115, 7713-7725.
15. D. Zhang, M. N. Slipchenko, D. E. Leaird, A. M. Weiner and J.-X. Cheng, *Optics express*, 2013, 21, 13864-13874.
16. J. P. Pezacki, J. A. Blake, D. C. Danielson, D. C. Kennedy, R. K. Lyn and R. Singaravelu, *Nat. Chem. Biol.*, 2011, 7, 137-145.
17. E. A. Gibson, O. Masihzadeh, T. C. Lei, D. A. Ammar and M. Y. Kahook, *Journal of ophthalmology*, 2011, 2011, 870879.
18. C. J. Strachan, M. Windbergs and H. L. Offerhaus, *Int. J. Pharm.*, 2011, 417, 163-172.
19. M. Vielreicher, S. Schurmann, R. Detsch, M. A. Schmidt, A. Buttgereit, A. Boccaccini and O. Friedrich, *J. R. Soc. Interface*, 2013, 10.
20. K. M. Hanson and C. J. Bardeen, *Photochem. Photobiol.*, 2009, 85, 33-44.
21. M. Müller and A. Zumbusch, *ChemPhysChem*, 2007, 8, 2156-2170.
22. M. Cnop, J. C. Hannaert, A. Hoorens, D. L. Eizirik and D. G. Pipeleers, *Diabetes*, 2001, 50, 1771-1777.
23. S. Martin and R. G. Parton, *Nature Reviews Molecular Cell Biology*, 2006, 7, 373-378.
24. J. C. Cohen, J. D. Horton and H. H. Hobbs, *Science*, 2011, 332, 1519-1523.
25. N. Ouchi, S. Kihara, Y. Arita, M. Nishida, A. Matsuyama, Y. Okamoto, M. Ishigami, H. Kuriyama, K. Kishida and H. Nishizawa, *Circulation*, 2001, 103, 1057-1063.
26. Y. Ohsaki, M. Suzuki and T. Fujimoto, *Chemistry & biology*, 2014, 21, 86-96.
27. L. L. Listenberger, X. Han, S. E. Lewis, S. Cases, R. V. Farese, D. S. Ory and J. E. Schaffer, *Proceedings of the National Academy of Sciences*, 2003, 100, 3077-3082.
28. L. L. Listenberger and D. A. Brown, *Current Biology*, 2008, 18, R237-R238.
29. S. Cermelli, Y. Guo, S. P. Gross and M. A. Welte, *Current Biology*, 2006, 16, 1783-1795.
30. Y. Miyanari, K. Atsuzawa, N. Usuda, K. Watashi, T. Hishiki, M. Zayas, R. Bartenschlager, T. Wakita, M. Hijikata and K. Shimotohno, *Nature cell biology*, 2007, 9, 1089-1097.
31. R. Mitra, O. Chao, Y. Urasaki, O. B. Goodman and T. T. Le, *BMC cancer*, 2012, 12, 540.
32. R. Mitra, O. B. Goodman and T. T. Le, *BMC cancer*, 2014, 14, 91.
33. J. Ramirez-Zacarias, F. Castro-Munozledo and W. Kuri-Harcuch, *Histochemistry*, 1992, 97, 493-497.

Analyst Accepted Manuscript

34. P. Greenspan, E. P. Mayer and S. D. Fowler, *The Journal of cell biology*, 1985, 100, 965-973.

35. L. Kuerschner, C. Moessinger and C. Thiele, *Traffic*, 2008, 9, 338-352.

36. K. Yen, T. T. Le, A. Bansal, S. D. Narasimhan, J.-X. Cheng and H. A. Tissenbaum, *PLoS One*, 2010, 5, e12810.

37. J. Zhu, B. Lee, K. K. Buhman and J.-X. Cheng, *Journal of lipid research*, 2009, 50, 1080-1089.

38. B. Lee, J. Zhu, N. E. Wolins, J.-X. Cheng and K. K. Buhman, *Biochimica et Biophysica Acta (BBA)-Molecular and Cell Biology of Lipids*, 2009, 1791, 1173-1180.

39. B. Lee, A. M. Fast, J. Zhu, J.-X. Cheng and K. K. Buhman, *Journal of lipid research*, 2010, 51, 1770-1780.

40. M. Bonn, M. Müller, H. A. Rinia and K. N. Burger, *Journal of Raman Spectroscopy*, 2009, 40, 763-769.

41. T. T. Le and J.-X. Cheng, *PLoS One*, 2009, 4, e5189.

42. M. N. Slipchenko, T. T. Le, H. Chen and J.-X. Cheng, *The Journal of Physical Chemistry B*, 2009, 113, 7681-7686.

43. T. T. Le, H. M. Duren, M. N. Slipchenko, C.-D. Hu and J.-X. Cheng, *Journal of lipid research*, 2010, 51, 672-677.

44. I. W. Schie and T. Huser, *Applied spectroscopy*, 2013, 67, 813-828.

45. J. P. Day, G. Rago, K. F. Domke, K. P. Velikov and M. Bonn, *Journal of the American Chemical Society*, 2010, 132, 8433-8439.

46. L. J. den Hartigh, J. E. Connolly-Rohrbach, S. Fore, T. R. Huser and J. C. Rutledge, *The Journal of Immunology*, 2010, 184, 3927-3936.

47. I. W. Schie, J. Wu, T. Weeks, M. A. Zern, J. C. Rutledge and T. Huser, *Journal of biophotonics*, 2011, 4, 425-434.

48. N. Argov, S. Wachsmann-Hogiu, S. L. Freeman, T. Huser, C. B. Lebrilla and J. B. German, *Journal of agricultural and food chemistry*, 2008, 56, 7446-7450.

49. B. Staels, J. Dallongeville, J. Auwerx, K. Schoonjans, E. Leitersdorf and J.-C. Fruchart, *Circulation*, 1998, 98, 2088-2093.

50. A. Uchida, M. N. Slipchenko, J.-X. Cheng and K. K. Buhman, *Biochimica et Biophysica Acta (BBA)-Molecular and Cell Biology of Lipids*, 2011, 1811, 170-176.

51. A. Uchida, M. C. Whitsitt, T. Eustaquio, M. N. Slipchenko, J. F. Leary, J.-X. Cheng and K. K. Buhman, *Frontiers in physiology*, 2012, 3.

52. W.-W. Chen, C.-H. Chien, C.-L. Wang, H.-H. Wang, Y.-L. Wang, S.-T. Ding, T.-S. Lee and T.-C. Chang, *Analytical and bioanalytical chemistry*, 2013, 405, 8549-8559.

53. M. A. Welte, *Current Biology*, 2004, 14, R525-R537.

54. X. Nan, E. O. Potma and X. S. Xie, *Biophysical journal*, 2006, 91, 728-735.

55. C. Jüngst, M. J. Winterhalder and A. Zumbusch, *Journal of biophotonics*, 2011, 4, 435-441.

56. C. Jüngst, M. Klein and A. Zumbusch, *Journal of lipid research*, 2013, 54, 3419-3429.

57. R. K. Lyn, D. C. Kennedy, S. M. Sagan, D. R. Blais, Y. Rouleau, A. F. Pegoraro, X. S. Xie, A. Stolow and J. P. Pezacki, *Virology*, 2009, 394, 130-142.

58. R. K. Lyn, D. C. Kennedy, A. Stolow, A. Ridsdale and J. P. Pezacki, *Biochemical and biophysical research communications*, 2010, 399, 518-524.

59. A. Zumbusch, G. R. Holtom and X. S. Xie, *Physical Review Letters*, 1999, 82, 4142.

60. E. Woodbury and W. Ng, 1962, vol. 50, pp. 2367-&.

61. M. C. Wang, W. Min, C. W. Freudiger, G. Ruvkun and X. S. Xie, *Nature methods*, 2011, 8, 135-138.

62. C. W. Freudiger, W. Min, G. R. Holtom, B. Xu, M. Dantus and X. S. Xie, *Nature photonics*, 2011, 5, 103-109.

63. W. Dou, D. Zhang, Y. Jung, J.-X. Cheng and D. M. Umulis, *Biophysical journal*, 2012, 102, 1666-1675.

64. L. Wei, Y. Yu, Y. Shen, M. C. Wang and W. Min, *Proceedings of the National Academy of Sciences*, 2013, 110, 11226-11231.

65. Y. Shen, F. Xu, L. Wei, F. Hu and W. Min, *Angewandte Chemie International Edition*, 2014, 53, 5596-5599.

66. T. Weeks, S. Wachsmann-Hogiu and T. Huser, *Optics express*, 2009, 17, 17044-17051.

67. T. Weeks, I. Schie, L. J. den Hartigh, J. C. Rutledge and T. Huser, *Journal of biomedical optics*, 2011, 16, 021117-021117-021115.

68. S. Hong, T. Chen, Y. Zhu, A. Li, Y. Huang and X. Chen, *Angewandte Chemie*, 2014, 126, 5937-5941.

69. L. Wei, F. Hu, Y. Shen, Z. Chen, Y. Yu, C.-C. Lin, M. C. Wang and W. Min, *Nature methods*, 2014.

70. X. Zhang, M. B. Roeffaers, S. Basu, J. R. Daniele, D. Fu, C. W. Freudiger, G. R. Holtom and X. S. Xie, *ChemPhysChem*, 2012, 13, 1054-1059.

71. C. L. Evans and X. S. Xie, *Annu. Rev. Anal. Chem.*, 2008, 1, 883-909.

72. C. Krafft, B. Dietzek and J. Popp, *Analyst*, 2009, 134, 1046-1057.

73. I. W. Schie and T. Huser, *Comprehensive Physiology*, 2013.

74. M. Monici, *Biotechnology annual review*, 2005, 11, 227-256.

75. D. Débarre, W. Supatto, A.-M. Pena, A. Fabre, T. Tordjmann, L. Combettes, M.-C. Schanne-Klein and E. Beaurepaire, *Nature methods*, 2005, 3, 47-53.

76. S. Witte, A. Negrean, J. C. Lodder, C. P. De Kock, G. T. Silva, H. D. Mansvelder and M. L. Groot, *Proceedings of the National Academy of Sciences*, 2011, 108, 5970-5975.

77. A. Alwan, *Global status report on noncommunicable diseases 2010*, World Health Organization, 2011.

78. F. H. Epstein and R. Ross, *New England journal of medicine*, 1999, 340, 115-126.

79. C. K. Glass and J. L. Witztum, *Cell*, 2001, 104, 503-516.

80. C. Weber and H. Noels, *Nature medicine*, 2011, 17, 1410-1422.

81. H. C. Stary, A. B. Chandler, R. E. Dinsmore, V. Fuster, S. Glagov, W. Insull, M. E. Rosenfeld, C. J. Schwartz, W. D. Wagner and R. W. Wissler, *Circulation*, 1995, 92, 1355-1374.

82. H.-W. Wang, I. M. Langohr, M. Sturek and J.-X. Cheng, *Arteriosclerosis, thrombosis, and vascular biology*, 2009, 29, 1342-1348.

83. L. B. Mostaço-Guidolin, M. G. Sowa, A. Ridsdale, A. F. Pegoraro, M. S. Smith, M. D. Hewko, E. K. Kohlenberg, B. Schattka, M. Shiomi and A. Stolow, *Biomedical optics express*, 2010, 1, 59-73.

84. S.-H. Kim, E.-S. Lee, J. Y. Lee, E. S. Lee, B.-S. Lee, J. E. Park and D. W. Moon, *Circulation research*, 2010, 106, 1332-1341.

85. R. S. Lim, J. L. Suhalim, S. Miyazaki-Anzai, M. Miyazaki, M. Levi, E. O. Potma and B. J. Tromberg, *Journal of lipid research*, 2011, 52, 2177-2186.

86. R. S. Lim, A. Kratzer, N. P. Barry, S. Miyazaki-Anzai, M. Miyazaki, W. W. Mantulin, M. Levi, E. O. Potma and B. J. Tromberg, *Journal of lipid research*, 2010, 51, 1729-1737.

87. H.-W. Wang, V. Simianu, M. J. Locker, J.-X. Cheng and M. Sturek, *Journal of biomedical optics*, 2011, 16, 021110-021110-021116.

88. J. L. Suhalim, C.-Y. Chung, M. B. Lilledahl, R. S. Lim, M. Levi, B. J. Tromberg and E. O. Potma, *Biophysical journal*, 2012, 102, 1988-1995.

89. C. Matthäus, S. Dochow, G. Bergner, A. Lattermann, B. Romeike, E. Marple, C. Krafft, B. Dietzek, B. Brehm and J. Popp, *Analytical Chemistry*, 2012, 84, 7845-7851.

90. G. Siegel, B. Agranoff, R. Albers, S. Fisher and M. Uhler, Philadelphia: Lippincott Williams and Wilkins. Copyright by American Society for Neurochemistry. www. ncbi. nlm. nih. gov/books/bv. fcgi, 2006.

91. F. P. Henry, D. Côté, M. A. Randolph, E. A. Rust, R. W. Redmond, I. E. Kochevar, C. P. Lin and J. M. Winograd, *Plastic and reconstructive surgery*, 2009, 123, 123S-130S.

92. J.-X. Cheng, S. Pautot, D. A. Weitz and X. S. Xie, *Proceedings of the National Academy of Sciences*, 2003, 100, 9826-9830.

93. E. Bèlanger, S. Bègin, S. Laffray, Y. De Koninck, R. Vallèe and D. Côtè, *Optics express*, 2009, 17, 18419-18432.

94. Y. Shi, W. Sun, J. J. McBride, J. X. Cheng and R. Shi, *Journal of neurochemistry*, 2011, 117, 554-564.

95. J. Imitola, D. Côté, S. Rasmussen, X. S. Xie, Y. Liu, T. Chitnis, R. L. Sidman, C. P. Lin and S. J. Khoury, *Journal of biomedical optics*, 2011, 16, 021109-021109-021111.

96. E. Bélanger, F. Henry, R. Vallée, M. Randolph, I. Kochevar, J. Winograd, C. Lin and D. Côté, *Biomedical optics express*, 2011, 2, 2698-2708.

97. Y. Fu, T. J. Frederick, T. B. Huff, G. E. Goings, S. D. Miller and J.-X. Cheng, *Journal of biomedical optics*, 2011, 16, 106006-106006-106010.

98. Y. Shi, D. Zhang, T. B. Huff, X. Wang, R. Shi, X.-M. Xu and J.-X. Cheng, *Journal of biomedical optics*, 2011, 16, 106012-106012-106014.

99. S. Bégin, E. Bélanger, S. Laffray, B. Aubé, É. Chamma, J. Bélisle, S. Lacroix, Y. De Koninck and D. Côté, *Biomedical optics express*, 2013, 4, 2003-2014.

100. M. Zimmerley, R. A. McClure, B. Choi and E. O. Potma, *Applied optics*, 2009, 48, D79-D87.

101. M. Zimmerley, D. C. Oertel, J. L. Ward, E. O. Potma, J. M. Marsh and C.-Y. Lin, *Journal of biomedical optics*, 2009, 14, 044019-044019-044017.

102. B. G. Saar, C. W. Freudiger, J. Reichman, C. M. Stanley, G. R. Holtom and X. S. Xie, *Science*, 2010, 330, 1368-1370.

103. B. G. Saar, L. R. Contreras-Rojas, X. S. Xie and R. H. Guy, *Molecular pharmaceutics*, 2011, 8, 969-975.

104. N. A. Belsey, N. L. Garrett, L. R. Contreras-Rojas, A. J. Pickup-Gerlaugh, G. J. Price, J. Moger and R. H. Guy, *Journal of Controlled Release*, 2014, 174, 37-42.

105. S. Heuke, N. Vogler, T. Meyer, D. Akimov, F. Kluschke, H. J. Röwert-Huber, J. Lademann, B. Dietzek and J. Popp, *British Journal of Dermatology*, 2013, 169, 794-803.

106. P. D. Chowdary, W. A. Benalcazar, Z. Jiang, D. M. Marks, S. A. Boppart and M. Gruebele, *Analytical chemistry*, 2010, 82, 3812-3818.

107. W. A. Benalcazar and S. A. Boppart, *Analytical and bioanalytical chemistry*, 2011, 400, 2817-2825.

108. K. König, H. Breunig, R. Bückle, M. Kellner-Höfer, M. Weinigel, E. Büttner, W. Sterry and J. Lademann, *Laser Physics Letters*, 2011, 8, 465.

109. H. G. Breunig, M. Weinigel, R. Bückle, M. Kellner-Höfer, J. Lademann, M. E. Darvin, W. Sterry and K. König, *Laser Physics Letters*, 2013, 10, 025604.

110. R. Mittal, M. Balu, T. Krasieva, E. O. Potma, L. Elkeeb, C. B. Zachary and P. Wilder-Smith, *Lasers in surgery and medicine*, 2013, 45, 496-502.

111. M. Windbergs, M. Jurna, H. L. Offerhaus, J. L. Herek, P. Kleinebudde and C. J. Strachan, *Analytical chemistry*, 2009, 81, 2085-2091.

112. M. N. Slipchenko, H. Chen, D. R. Ely, Y. Jung, M. T. Carvajal and J.-X. Cheng, *Analyst*, 2010, 135, 2613-2619.

113. C. M. Hartshorn, Y. J. Lee, C. H. Camp Jr, Z. Liu, J. Heddleston, N. Canfield, T. A. Rhodes, A. R. Hight Walker, P. J. Marsac and M. T. Cicerone, *Analytical chemistry*, 2013, 85, 8102-8111.

114. G. Bergner, C. R. Albert, M. Schiller, G. Bringmann, T. Schirmeister, B. Dietzek, S. Niebling, S. Schlücker and J. Popp, *Analyst*, 2011, 136, 3686-3693.

115. S. Bott and R. Kirby, *Prostate cancer and prostatic diseases*, 2001, 5, 252-263.

116. T. M. Pawlik, C. R. Scoggins, D. Zorzi, E. K. Abdalla, A. Andres, C. Eng, S. A. Curley, E. M. Loyer, A. Muratore and G. Mentha, *Annals of Surgery*, 2005, 241, 715.

117. S. E. Singletary, *The American journal of surgery*, 2002, 184, 383-393.

118. N. Vogler, T. Meyer, D. Akimov, I. Latka, C. Krafft, N. Bendsoe, K. Svanberg, B. Dietzek and J. Popp, *Journal of biophotonics*, 2010, 3, 728-736.

119. N. Vogler, A. Medyukhina, I. Latka, S. Kemper, M. Böhm, B. Dietzek and J. Popp, *Laser Physics Letters*, 2011, 8, 617.

120. Y. Yang, F. Li, L. Gao, Z. Wang, M. J. Thrall, S. S. Shen, K. K. Wong and S. T. Wong, *Biomedical optics express*, 2011, 2, 2160-2174.

121. T. Meyer, N. Bergner, C. Bielecki, C. Krafft, D. Akimov, B. F. Romeike, R. Reichart, R. Kalff, B. Dietzek and J. Popp, *Journal of biomedical optics*, 2011, 16, 021113-021113-021110.

122. T. Meyer, O. Guntinas-Lichius, F. von Eggeling, G. Ernst, D. Akimov, M. Schmitt, B. Dietzek and J. Popp, *Head & neck*, 2013, 35, E280-E287.

123. X. Xu, J. Cheng, M. J. Thrall, Z. Liu, X. Wang and S. T. Wong, *Biomedical optics express*, 2013, 4, 2855-2868.

124. R. Galli, V. Sablinskas, D. Dasevicius, A. Laurinavicius, F. Jankevicius, E. Koch and G. Steiner, *Journal of Biophotonics*, 2014, 7, 23-27.

Analyst Accepted Manuscript

125. C. W. Freudiger, R. Pfannl, D. A. Orringer, B. G. Saar, M. Ji, Q. Zeng, L. Ottoboni, W. Ying, C. Waeber and J. R. Sims, *Laboratory investigation*, 2012, 92, 1492-1502.

126. M. Ji, D. A. Orringer, C. W. Freudiger, S. Ramkissoon, X. Liu, D. Lau, A. J. Golby, I. Norton, M. Hayashi and N. Y. Agar, *Science translational medicine*, 2013, 5, 201ra119-201ra119.

127. C. Pohling, T. Buckup, A. Pagenstecher and M. Motzkus, *Biomedical optics express*, 2011, 2, 2110-2116.

128. C. H. Camp Jr, Y. J. Lee, J. M. Heddleston, C. M. Hartshorn, A. R. H. Walker, J. N. Rich, J. D. Lathia and M. T. Cicerone, *arXiv preprint arXiv:1402.3211*, 2014.

129. H. H. Tu and S. A. Boppart, *Journal of Biophotonics*, 2014, 7, 9-22.

130. M. Baumgartl, T. Gottschall, J. Abreu-Afonso, A. Diez, T. Meyer, B. Dietzek, M. Rothhardt, J. Popp, J. Limpert and A. Tunnermann, *Opt Express*, 2012, 20, 21010-21018.

131. T. Meyer, M. Baumgartl, T. Gottschall, T. Pascher, A. Wuttig, C. Matthaus, B. F. M. Romeike, B. R. Brehm, J. Limpert, A. Tuennermann, O. Guntinas-Lichius, B. Dietzek, J. U. Popp and J. Popp, *Analyst*, 2013, 138, 4048-4057.

132. S. Murugkar, B. Smith, P. Srivastava, A. Moica, M. Naji, C. Brideau, P. K. Stys and H. Anis, *Opt Express*, 2010, 18, 23796-23804.

133. M. Balu, G. Liu, Z. Chen, B. J. Tromberg and E. O. Potma, *Optics Express*, 2010, 18, 2380-2388.

134. B. G. Saar, R. S. Johnston, C. W. Freudiger, X. S. Xie and E. J. Seibel, *Optics Letters*, 2011, 36, 2396-2398.
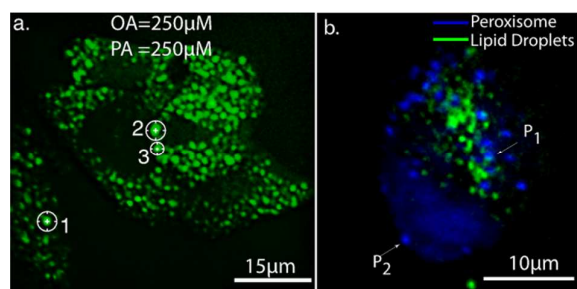
This review provides an update on coherent Raman scattering microscopy of cells and tissues since 2008 including CARS and SRS.